Materials Horizons

ROYAL SOCIETY OF CHEMISTRY

COMMUNICATION

View Article Online
View Journal | View Issue

Cite this: *Mater. Horiz.*, 2024, **11**, 1098

Received 1st September 2023,
Accepted 30th November 2023

DOI: 10.1039/d3mh01393f

rsc.li/materials-horizons

Kirkendall effect induced ultrafine VOOH nanoparticles and their transformation into VO_2(M) for energy-efficient smart windows†

Liangfei Wu,‡[a] Antonio Teng,‡[b] Ming Li,*[ac] Liang Li,[ac] Zhulin Huang,[ac] Xinyang Li,[a] Jie Yu,[a] Sichao Xu,[a] Fengxia Zou,[ac] Andy Zou,[d] Jinghui Zhang,[ef] Tao Jiang,[ef] Ye Xin,[g] Xiaoye Hu*[ac] and Guanghai Li*[ac]

Vanadium dioxide (VO_2) has received widespread attention for application in energy-efficient smart windows because of its distinct thermochromic property in the near-infrared region during the reversible metal–insulator phase transition. In this study, lepidocrocite VOOH ultrafine nanoparticles (NPs) with a diameter less than 30 nm were prepared by a mild and efficient hydrothermal method, and the Kirkendall effect played a vital role in the growth of the VOOH NPs. It was found that VOOH could be transformed into VO_2 *via* a subsequent annealing treatment during which the size and morphology of VOOH are well preserved even though the annealing temperature is up to 500 °C. The ultrafine VO_2 NPs are crucial for achieving excellent nanothermochromic performance with a luminous transmittance (T_{lum}) up to 56.45% and solar modulation ability (ΔT_{sol}) up to 14.95%. The environmental durability is well improved by coating VO_2 NPs with an SiO_2 shell as confirmed *via* progressive oxidation and acid corrosion experiments. Meanwhile, the T_{lum} of the VO_2@SiO_2 film is further increased from 56.45% to 62.29% while the ΔT_{sol} remained unchanged. This integrated thermochromic performance presents great potential for the development of VO_2-based smart windows.

New concepts

VO_2 has a unique dynamic thermochromic property that can be exploited in energy-efficient smart windows with the aim of maintaining comfortable living surroundings without the excessive use of air-conditioning. Hydrothermal synthesis is a powerful method to obtain high-performance VO_2 nanostructures for nanothermochromic coatings, but it still suffers from time-consumption and high reaction temperatures. In this study, newly reported lepidocrocite VOOH nanoparticles of about 25 nm were prepared for the first time *via* an efficient and mild hydrothermal route. The Kirkendall effect was found to be a critically important feature in the formation of ultrafine VOOH NPs. The phase transition from VOOH to VO_2(M) was studied by annealing in order to obtain the thermochromic performance. Both the reduced particle size and localized surface plasmon resonance (LSPR) absorption gave rise to the enhanced thermochromic property of VO_2 with a T_{lum} of 56.45% and ΔT_{sol} of 14.95%. After coating VO_2 with an amorphous SiO_2 shell, the T_{lum} was further increased up to 62.29% while the ΔT_{sol} had no degradation. The outstanding thermochromic performance and enhanced environmental durability of VO_2 will pave the way forward for the development of energy-efficient smart windows.

1. Introduction

Building energy consumption accounts for ~40% of total global energy consumption, and a major part of this energy (~60%) is lost through windows in the building because of the superabundant solar radiation transmitted through the window increasing the indoor cooling and heating loads for air conditioners in summer and winter, respectively.[1–3] Therefore, the use of smart windows that can dynamically regulate the amount of solar transmission in response to an external stimulus could have a significant positive effect on energy savings. Diverse smart windows have been achieved using mechano, thermo, electro, or photo stimuli. The thermochromic smart window provides a new, intriguing option owing to its structural simplicity and does not require any additional energy consumption to achieve more energy savings.[4–6]

VO_2 is the most widely studied thermochromic material and exhibits an obvious reversible phase transition from a

[a] *Key Laboratory of Materials Physics, Anhui Key Laboratory of Nanomaterials and Nanotechnology, Institute of Solid State Physics, Hefei Institutes of Physical Science, Chinese Academy of Sciences, Hefei 230031, P. R. China. E-mail: liming@issp.ac.cn, hxy821982@issp.ac.cn, ghli@issp.ac.cn*
[b] *ContiTech ChinaRubber & Plastics Technology Ltd, Changshu 215500, P. R. China*
[c] *University of Science and Technology of China, Hefei 230026, P. R. China*
[d] *Benecke Changshun Auto Trim Co., Ltd., Zhangjiagang 215632, P. R. China*
[e] *Key Laboratory of Atmospheric Optics, Anhui Institute of Optics and Fine Mechanics, Hefei Institutes of Physical Science, Chinese Academy of Sciences, Hefei 230031, P. R. China*
[f] *Advanced Laser Technology Laboratory of Anhui Province, Hefei 230037, P. R. China*
[g] *Naval Research Institute, Beijing 102442, P. R. China*

† Electronic supplementary information (ESI) available. See DOI: https://doi.org/10.1039/d3mh01393f

‡ The authors have equally contributed to this work.

monoclinic (M) insulator phase to a rutile (R) metallic phase at a critical temperature of ~340 K. The structural phase transition is accompanied by a dramatic change of optical property: VO_2(R) is highly reflective to infrared radiation, while VO_2(M) exhibits optical transparency in the infrared band.[7,8] It is worth mentioning that the phase transition can block heat radiation without shading the glazing because the luminous transmittance is of nearly the same value for both VO_2(R) and VO_2(M). In addition, the percolative nature of the thermally-induced phase transition in VO_2 allows for designing devices with a self-adaptive property, eliminating the need for human intervention or additional energy supply for external control. Hence, thermochromic smart windows based on VO_2 provide real intelligent control over infrared modulation. For practical applications, both the luminous transmittance (T_{lum}) and solar modulation ability (ΔT_{sol}) are important parameters that determine the thermochromic performance of VO_2 coatings used in smart windows. An ideal thermochromic coating should be highly transparent in the visible region, and the variation of infrared modulation associated with the phase change should be as high as possible. In other words, the higher both T_{lum} and ΔT_{sol}, the better the application prospects of VO_2 coatings. Unfortunately, a higher T_{lum} is usually at the expense of an extremely low ΔT_{sol} and *vice versa*. Therefore, the major challenge for VO_2-based smart windows is to simultaneously improve the T_{lum} (> 60%) and ΔT_{sol} (> 12%).

Several strategies have been deployed to overcome the trade-off of ΔT_{sol} and T_{lum}, such as porous films, nanothermochromic coatings, bio-inspired structure, multilayer anti-reflective film, and so on.[9–11] Most experimental data and theoretical results demonstrate that, of the nanothermochromic coatings, VO_2 NPs dispersed in a glass or polymer matrix outperformed all the other methods since the subwavelength VO_2 NPs can reduce light scattering and increase transmittance. In this case, the particle size, dispersibility and crystallinity of VO_2 NPs play a vital role in affecting the optical properties of VO_2-based smart windows. Additionally, the ultrafine VO_2 NPs exhibit superior modulation of ΔT_{sol} and T_{lum} due to plasmonic effects when the NPs are in their metallic state. Thus, reducing the particle size and improving the crystallinity of VO_2 have been the focus of recent research. However, to date, a simple and practical method for producing ultrafine high-quality VO_2 NPs is still lacking, especially as it is in high demand to selectively control the size, dispersibility and degree of crystallinity of VO_2.

V exhibits a wide range of oxidation states, and VO_2 has a number of polymorphic forms, such as VO_2(M), VO_2(M_2), VO_2(R), VO_2(A), VO_2(B), and VO_2(D). Thus, the choice of preparation method is particularly important to obtain the specific thermochromic phase of VO_2(M) or VO_2(R). The hydrothermal method has been shown to be the most suitable method to synthesize high-quality VO_2 NPs with controllable crystal structure, morphology and crystallinity by adjusting simple parameters such as reaction temperature, precursor concentration, pH and hydrothermal time. But, in most cases, the hydrothermal products are usually a metastable phase of VO_2(B) or VO_2(A).[12,13] Even though a few reports have studied one-step hydrothermal synthesis of VO_2(M), the preparation conditions were harsh, such as a higher reaction temperature (> 240 °C) and a longer hydrothermal time (> 24 h). Hence, some special intermediate phases like VO_2(D), VO_2(P) and $VC_2H_4O_3$ have been prepared first by mild hydrothermal method and then an extra annealing process is applied to obtain VO_2(M).[14–16] It is important to highlight that the mild hydrothermal conditions and annealing process are both beneficial to obtaining the nanostructure as well as improving the crystallinity of VO_2(M), which provides an alternative route to overcome the Achilles heels of overgrowth and low crystallization of VO_2 NPs. Amongst the above-mentioned special intermediate phases, VOOH exhibits a number of polymorphic forms, such as α-VOOH, montroseite VOOH and lepidocrocite VOOH. However, nearly all studies about them and their derivatives focus on the electrochemical fields, such as lithium-ion batteries, water electrolysis and supercapacitors.[17–20] Moreover, as an intermediate product, all reported VOOH are larger than 100 nm in size, which is far from being able to meet the needs of VO_2-based smart windows. Thus, it is meaningful to prepare ultrafine VOOH NPs and investigate their phase transformation behavior from VOOH to VO_2(M), which could develop and enrich the mild strategy for preparing nanothermochromic VO_2(M).

In this paper, we demonstrated a mild hydrothermal method to prepare lepidocrocite VOOH NPs with diameters less than 40 nm and the Kirkendall effect was responsible for the formation of the ultrafine NPs. Importantly, the VOOH NPs could be converted to VO_2(M) with no significant size change during the annealing treatment even though the annealing temperature was up to 500 °C. The nanothermochromic films on glass substrates were prepared by incorporating VO_2(M) NPs into a PVP (polyvinylpyrrolidone) matrix, which presented a T_{lum} of 56.45% and ΔT_{sol} of 14.95%. Moreover, the optical performance and environmental durability could be further enhanced by coating a SiO_2 shell on the VO_2(M) NPs. The as-prepared VO_2@SiO_2/PVP films exhibited outstanding thermochromic performance with an enhanced T_{lum} of 62.29% and ΔT_{sol} of 14.91%, showing great potential for practical application in energy-efficient smart windows.

2. Experimental section

Materials

The solvents and chemicals, including ammonium metavanadate (NH_4VO_3), hydrochloric acid (HCl, 37%), hydrazine hydrate aqueous solution ($H_4N_2{\cdot}H_2O$, 85%), formic acid (HCOOH, 88 wt%), ammonia water ($NH_3{\cdot}H_2O$, 28 wt%), tetraethyl orthosilicate (TEOS), and PVP K30, were used without further purification.

Preparation of lepidocrocite VOOH ultrafine NPs

Lepidocrocite VOOH ultrafine NPs were prepared *via* hydrothermal method. Briefly, 0.234 g NH_4VO_3 was added into 30 mL deionized water under magnetic stirring at room temperature until the solution became transparent. Later, 2 ml 1 M HCl, 1 ml HCOOH and 2 ml $H_4N_2{\cdot}H_2O$ were added in turn.

After stirring for 30 min, the suspension was hydrothermally treated at 160 °C for 6 h. The black product was collected by centrifugation, washed with ethanol and dried at 60 °C in vacuum. The specific values for the constant parameters for different gradient experiments are shown in Fig. S1 (ESI†).

Preparation of core–shell VO_2(M)@SiO_2 NPs

In order to transform VOOH into VO_2(M), the VOOH NPs were heated at 500 °C for 1 h in a vacuum of ~1 Pa. The obtained blue-black powder was dispersed into 60 ml ethanol and sonicated for 1 h. 10 ml deionized water, 4 ml 28 wt% concentrated ammonia solution and 0.2 (S1), 0.5 (S2) or 1 ml (S3) TEOS were added sequentially and slowly into the above dispersions under stirring for 1 h. Finally, the product was washed with ethanol and collected by centrifugation.

Preparation of VO_2-based coatings

0.27 g VO_2(M) or VO_2@SiO_2, 0.27 g PVP K30, and 10 ml ethanol were well mixed by means of ball milling. Before spin coating, the glass substrates (25 × 25 mm^2) were cleaned with acetone, ethanol and deionized water sequentially to remove surface contamination and were finally dried at room temperature. Then, 0.2 ml dispersion was deposited on the glass and then spin-coated at a speed of 1500 rpm for 30 s. The thickness of the film can be changed by varying the number of spinning times. The preparation process is illustrated in Fig. 1a.

Characterization

The morphology and phase structure of the NPs were examined using field-emission scanning electron microscopy (FESEM, Hitachi SU8020) and X-ray diffraction with a Cu Ka1 line (XRD, PANalytical X'Pert). High resolution TEM analysis was carried out using an image aberration corrected TEM (JEOL JEM-2010). A low accelerating voltage of 80 kV was used in order to avoid beam irradiation induced damage. The phase transition behaviors were analyzed using a differential scanning calorimeter (DSC, PerkinElmer) at a heating rate of 10 °C min^{-1} in a flowing nitrogen atmosphere. Optical transmission spectra were recorded using a UV-3600 spectrophotometer (Shimadzu UV3600-MPC3100) equipped with a temperature controller.

To assess the visual and energy saving performance of all the films, the integral luminous transmittance (T_{lum}, 380–780 nm)

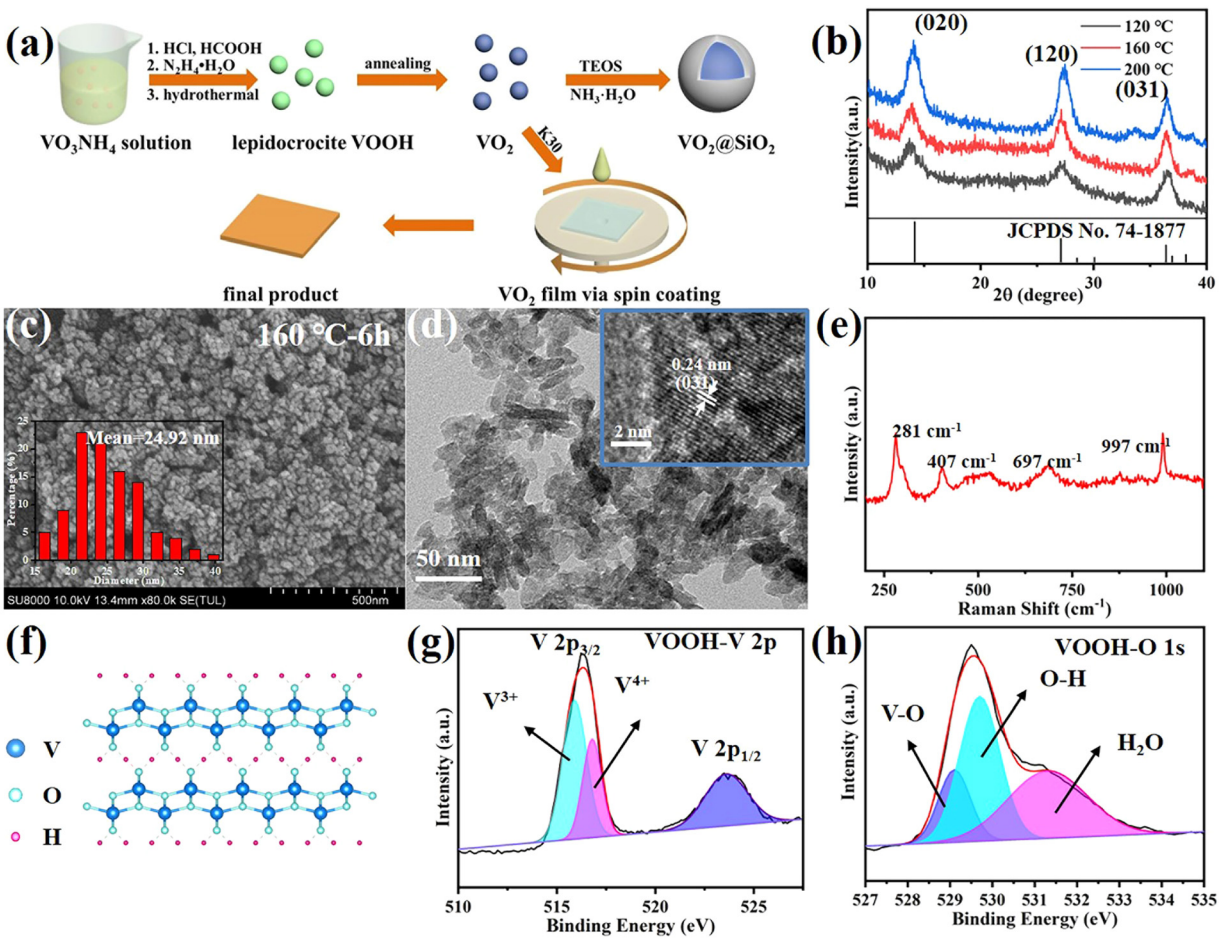

Fig. 1 (a) Sample preparation flow illustrations. (b) XRD patterns of VOOH NPs prepared at different hydrothermal temperatures. (c) SEM and (d) TEM images of VOOH NPs prepared at hydrothermal temperature of 160 °C for 6 h. (e) Raman spectra and (f) geometric structure of VOOH NPs. XPS analysis of VOOH: (g) V 2p and (h) O 1s. (Inset: histogram of size distribution (c) and HR-TEM image (d) of the VOOH NPs).

and solar transmittance (T_{sol}, 250–2500 nm) were calculated using the following equation,

$$T_{lum(sol)} = \frac{\int \varphi_{lum(sol)}(\lambda) T(\lambda) d\lambda}{\int \varphi_{lum(sol)}(\lambda) d\lambda}$$

where $T(\lambda)$ represents the transmittance at wavelength λ, $\varphi_{lum}(\lambda)$ is the spectral sensitivity of the light-adapted eye, and $\varphi_{sol}(\lambda)$ is the solar irradiance spectrum for air mass 1.5 corresponding to the sun standing 37° above the horizon. As a result, the solar modulation efficiency ΔT_{sol} could be calculated by

$$T_{sol} = T_{sol,lt} - T_{sol,ht}$$

where lt and ht represent 25 and 100 °C, respectively.

Simulation

The three-dimensional finite difference time domain (FDTD) method was used to simulate the optical performance of VO_2@SiO_2. The radius of VO_2 was 20 nm and the shell thickness was 11 nm. PML (perfectly matched layer) boundary conditions were set for the Z direction. Periodic boundary conditions were applied in the X and Y directions. The plane wave (300 nm–2500 nm) was incident perpendicular to the structure along the Z direction. Power monitors were placed at fixed Z positions below the VO_2 to detect the transmitted beam intensity.

3. Results and discussion

Lepidocrocite ultrafine VOOH NPs

In our work, by adjusting some hydrothermal parameters, including the volume of HCOOH as well as the hydrothermal temperature and reaction time, it was possible to alter the characteristics of the VOOH particles, such as size, morphology and crystalline phase. To study the synthesis temperature's influence on the hydrothermal products, a gradient experiment was performed by varying the synthesis temperature from 80 °C to 200 °C with a temperature interval of 40 °C. Fig. 1b displays the XRD patterns of VOOH NPs prepared under different hydrothermal temperatures. The diffraction peaks at 2θ = 14°, 27° and 36.4° matched well with the (020), (120) and (031) crystalline planes of lepidocrocite FeOOH (JCPDS card no. 74–1877), and no other phases of vanadium oxides were detected, indicating lepidocrocite VOOH NPs were prepared successfully.[21] It was clear that the diffraction peaks became stronger with a higher temperature due to the enhanced crystallinity. In the SEM images (Fig. 1c and Fig. S2a, b, ESI†), all three VOOH NPs with uniform size <40 nm were clearly discernable and the one obtained at 160 °C presented the smallest average size of 24.92 nm (measured by Nano Measurer 1.2 software). Notably, Fig. S2c, d (ESI†) indicated VOOH NPs could not be obtained with a lower hydrothermal temperature of 80 °C. The ultrafine VOOH NPs were further confirmed by the TEM images shown in Fig. 1d, of which the high-resolution TEM image indicated that the lattice spacing is 0.24 nm, consistent with the (031) plane of VOOH. Considering the similar shapes and sizes between the samples synthesized in these experiments, it could be concluded that the synthesis temperature in a wide range had a limited effect on the morphology and size of the obtained VOOH NPs. For further characterization, the structure of VOOH was determined from Raman spectroscopy, as seen in Fig. 1e, and the characteristic layer structure was observed at 281 cm^{-1}, which was consistent with the crystal structure of VOOH shown in Fig. 1f.[19] The oxidation state of VOOH was investigated by X-ray photoelectron spectroscopy (XPS). For the valence states of V, in addition to V^{3+} (515.9 eV) from the V 2p spectra of VOOH, V^{4+} (516.8 eV) could be also found, suggesting that the V^{3+} was partially oxidized due to exposure to air (Fig. 1g). In the O 1s spectrum of VOOH, the three peaks located at 529, 529.6 and 531.3 eV were assigned to O^{2-} in V–O, O–H and H_2O, respectively (Fig. 1h). Combined with the above results, it could be concluded that lepidocrocite VOOH ultrafine NPs were obtained after the hydrothermal reaction.

Besides the reaction temperature, the influence of the addition of HCOOH on the morphology of VOOH was also evaluated during the hydrothermal process. We fixed the total volume of acid at 3 ml and changed the volume of HCOOH from 0 to 2 ml. The SEM images of the different hydrothermal products are shown in Fig. S3a–d (ESI†). In Fig. S3a (ESI†), micron-sized hollow spheres can be found when no HCOOH was added and this was a common shape of VOOH in previous research work.[17] As the amount of HCOOH increased, the size of the particles decreased gradually. However, the particle size increased inversely when the HCOOH content was greater than 1 ml. Particularly, when the amount of HCOOH was 2 ml, the resulting hydrothermal product was irregular micron-sized particles. Moreover, the SEM images of the solid precipitates before hydrothermal treatment with different volumes of HCOOH are displayed in Fig. S4a–d (ESI†). Fig. S4e (ESI†) shows the digital photographs of the corresponding hydrothermal precursor solution before and after centrifugation. It was noteworthy that, when the content of HCOOH was 2 ml, there was no precipitate formed and the solution was a clear azure color, which may be attributed to the presence of aqueous tetravalent vanadium in the form of vanadyl ions (VO^{2+}).[22] At the same time, a small amount of VO^{2+} was generated when the HCOOH content was 1.5 ml, which can be inferred from the color of the precursor solution after centrifugation. In this case, the coexistence of VO^{2+} and solid precipitates may be responsible for the paradoxical increase in the size of hydrothermal product. Otherwise, by comparing the SEM images before and after hydrothermal treatment, it can be assumed that there was a positive correlation between the size of the hydrothermal product and the hydrothermal precursor, while the main function of HCOOH was to reduce the size of the precursor, thus promoting the formation of ultrafine VOOH NPs.

The reaction time was also examined for insight into the formation process of VOOH NPs. The XRD patterns in Fig. 2a suggested that 1.5 h was enough for the formation of lepidocrocite VOOH when the hydrothermal temperature was 160 °C, even though ultrafine VOOH NPs had a tendency to agglomerate (Fig. 2b). It gave us a hint that the hydrothermal time could be further shortened. However, the precursors could not be

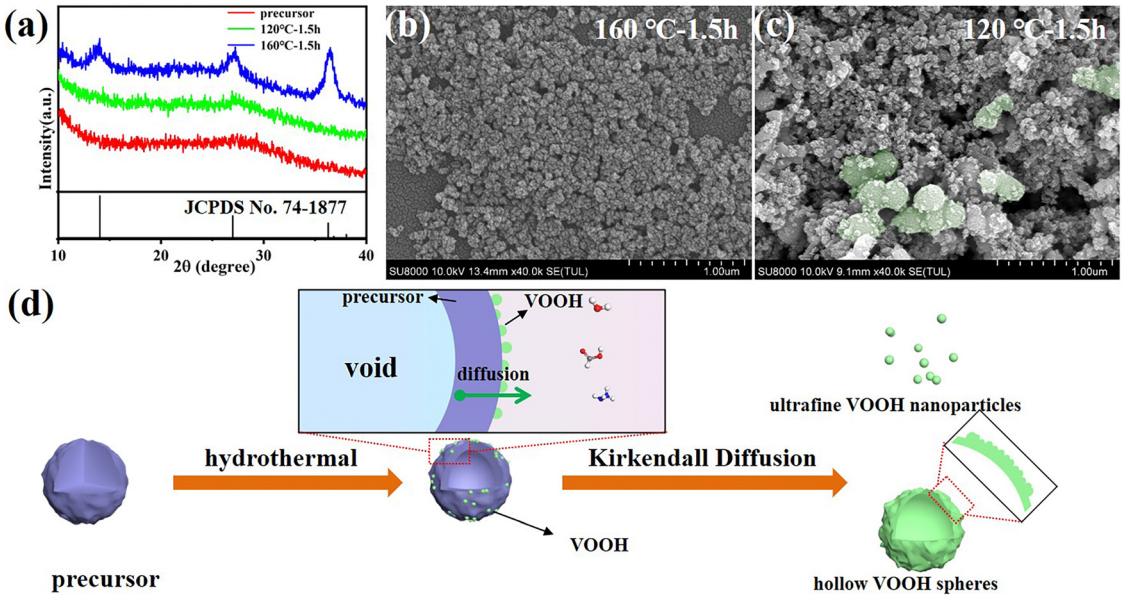

Fig. 2 (a) XRD patterns of hydrothermal precursor and hydrothermal products. SEM images of hydrothermal products under different conditions: (b) 160 °C-1.5 h and (c) 120 °C-1.5 h. (d) Schematic illustrations of Kirkendall diffusion process and the formation of ultrafine VOOH NPs.

totally converted into VOOH when the hydrothermal temperature was 120 °C, because the amorphous peak at ~28° belonging to the amorphous precursor was maintained (Fig. 2a). As shown in Fig. 2c, some VOOH NPs can be found adhered to the precursor surface, indicating that the VOOH NPs generated at the precursor/solution interface. Based on the above characterization, a diagram to depict the formation of ultrafine VOOH NPs is illustrated in Fig. 2d. At the beginning of the hydrothermal process, the hydrolyzation reaction at the precursor/solution interface occurred to form a loosely packed VOOH shell. This process was coupled with a continuous outward flow of the core structure of the precursor based on the Kirkendall effect, where voids can be formed due to differences in diffusion direction and speed between different ions in the synthesis process.[23–26] The Kirkendall effect usually occurs in one-step, relatively facile processes that do not require template removal to prepare hollow-structured nanomaterials, but it seemed to be somewhat different in this work. For precursors with larger particle sizes, there was sufficient core mass to sustain the transport process and a relatively compact shell was formed which corresponded to the SEM image in Fig. S3a (ESI†). For precursors with smaller particle sizes, the core mass was insufficient to create effective connections between the initial VOOH NPs randomly distributed on the surface of the precursor, leading to the generation of isolated VOOH NPs. At the same time, a higher hydrothermal temperature not only helped to accelerate the reaction process, but also provided more active sites for the reaction, further reducing the particle size of VOOH. The increase in particle size of VOOH at a hydrothermal temperature of 200 °C might be related to the solid-solution-solid mechanism, which induces the anisotropic growth of VOOH to form a flake structure and is confirmed in Fig. S5 (ESI†).

Transformation from VOOH to VO_2(M)

VOOH can react with O_2 to form VO_2 according to the following formula.

$$4VOOH + O_2 \xrightarrow{\Delta} 4VO_2 + 2H_2O$$

In accordance with the above equation, appropriate oxygen content is necessary to obtain VO_2. Therefore, the VOOH NPs were thermally annealed under a vacuum of ~1 Pa at a temperature of 500 °C. Different annealing times were applied to study the phase structure and morphology evolution during vacuum annealing. Fig. 3a displays the XRD patterns of samples with an annealing time increase from 20 to 150 min. All diffraction peaks matched well with the standard card JCPDS No. 43-1051, indicating that the pure monoclinic VO_2(M) phase was successfully synthesized.[27,28] The SEM images of VO_2 NPs with different annealing times are shown in Fig. 3b and Fig. S6a–d (ESI†). It was found that the diameter of VO_2 NPs increased with prolonged annealing time and that significant coalescence events only occurred with annealing times above 2 h. Fig. S7 (ESI†) and Fig. 3c present the TEM images of VO_2 NPs annealed for 20 and 60 min, respectively. Most of the VO_2 NPs were isolated with a few particles starting to coalesce (circled by the white line), but the particle size was still small enough to be considered ultrafine VOOH. Fig. 3d reveals the crystalline structure of VO_2 with clear lattice fringes. The calculated interplanar spacing was ~0.32 nm, which matched well with the lattice spacing of the (011) plane.[29,30] In order to investigate the structural phase change from VOOH to VO_2, different annealing temperatures and vacuum degrees were also employed. Fig. S8a (ESI†) displays the XRD patterns of VO_2 with different annealing temperatures. It was found that VOOH was first transformed into VO(A) and then to VO_2(M)

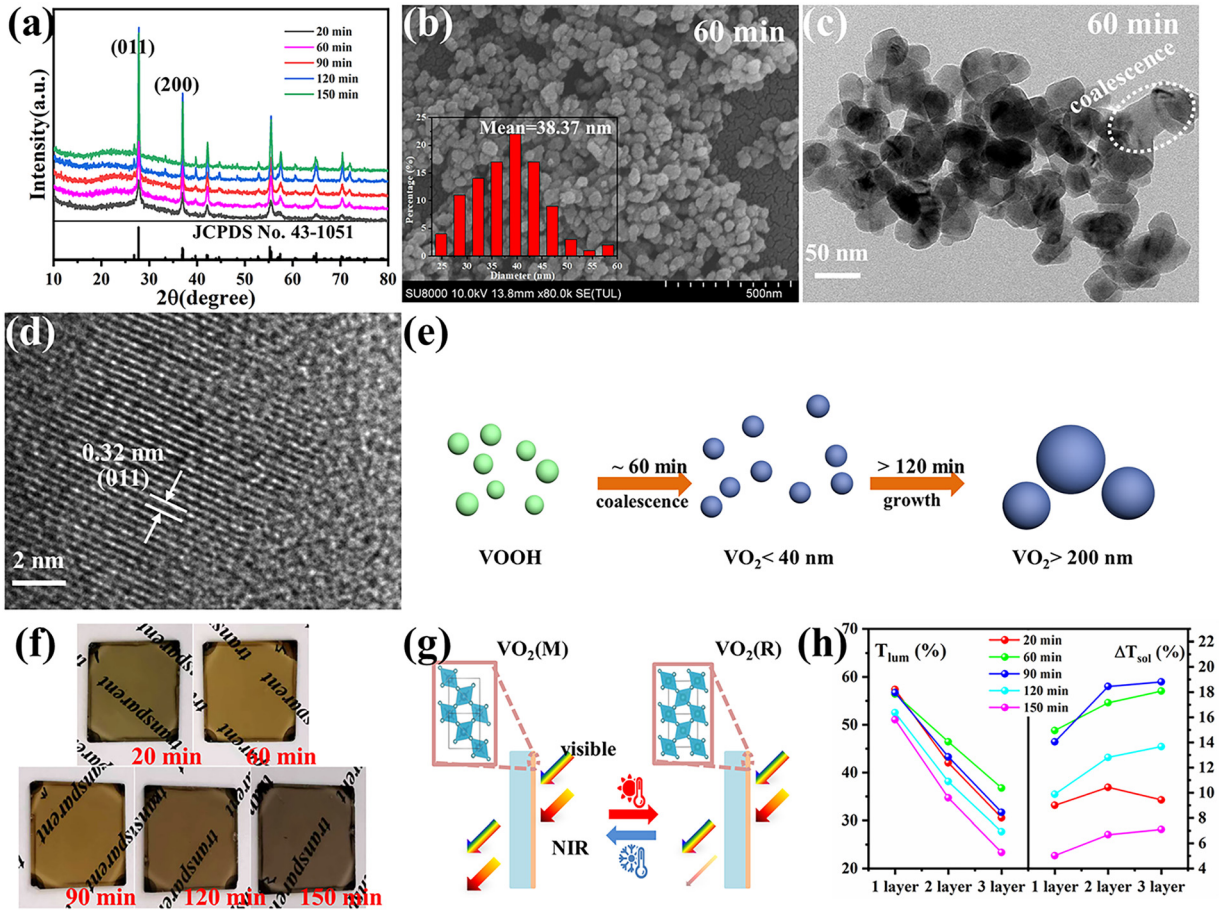

Fig. 3 (a) XRD patterns of VO_2 with different annealing times. (b) SEM and (c) and (d) TEM images of VO_2 with annealing a time of 60 min. (e) Schematic illustrations of the transformation of VOOH into VO_2. (f) Digital images of VO_2/PVP films. (g) Working principle of the VO_2-based smart window. (h) The optical performances of VO_2/PVP films with various spin coating times. (Inset (b): histogram of size distribution of the VO_2 NPs).

when the annealing temperature increased from 350 °C to 450 °C. The SEM images of the annealed products at different annealing temperatures are displayed in Fig. S8b–d (ESI†). All three samples presented similar sizes, suggesting that annealing temperature had a minor effect on the morphologies. Fig. S9a (ESI†) displays the XRD patterns of VO_2 with different vacuum degrees. O_2 was necessary for the transformation from VOOH to VO_2, thus only V_3O_5 was obtained at 0 Pa. VO_2(M) was obtained when the vacuum degree was increased to 3 Pa or 6 Pa. However, the particle sizes of the prepared VO_2 were about 150 nm under these conditions, which was not conducive to optical performance. Fig. S10 (ESI†) further confirms that different hydrothermal products could also be successfully transformed into VO_2 after annealing at 500 °C with a vacuum degree of 1 Pa for 1 h. The phase transition property of the VO_2 powder was further analyzed by DSC, as shown in Fig. S11 (ESI†). When VOOH was annealed for 20 min, the phase transition temperature of T_c was 64.62 °C which increased to ~80 °C when VOOH was annealed for a longer time. That was because the defects generated during the transformation process from VOOH to VO_2 and the defect density were reduced with the increase of annealing time. Thus, a relatively large supercooling/superheating degree was necessary to drive the phase transition, which resulted in a large thermal hysteresis (the temperature gap between the exothermic peak and endothermic peak). It is worth noting that when the heat treatment time was 120 min, multiple exothermic peaks emerged, suggesting the coexistence of different types of VO_2 NPs, which is consistent with the corresponding SEM images in Fig. S6c (ESI†). Based on the above characterization, it could be concluded that the formation and coalescence of VO_2 occur simultaneously (Fig. 3e). As long as the annealing treatment time was controlled properly, VO_2 with good crystallinity and fine particle size less than 40 nm could be obtained easily, which is crucial for optimizing the optical properties of VO_2-based thermochromic films.

For practicality, VO_2 NPs were dispersed into a PVP matrix and then coated onto glass substrates to form VO_2-based films. Fig. 3f displays the digital images of the VO_2/PVP films. Both shorter (20 min) and longer (120 and 150 min) annealing times for VO_2 caused the films to become dark. The two cases in this study were due to the presence of residual VOOH for the former and the strong Mie scattering from the large particle size of VO_2 for the latter.[13] An appropriate annealing time (60 and 90 min) led to the film exhibiting the typical yellow-brown color belonging to VO_2(M). The SEM image for the surface morphology of

the VO_2/PVP-60 min film is presented in Fig. S12a (ESI†) and the white dots are VO_2 grains. The inset AFM image in Fig. S12a (ESI†) displays a surface roughness of 11.87 nm for the film. The cross-sectional image in Fig. S12b (ESI†) further reveals the thickness of the film to be around 400 nm. The optical modulation properties of the VO_2/PVP films were investigated to evaluate their potential for usage in smart windows by measuring the transmittance spectra at 25 °C and 100 °C (Fig. S13a–e, ESI†). The corresponding T_{lum} and ΔT_{sol} are summarized in Fig. 3h and Fig. S14 (ESI†). For all VO_2 films, the thicker films exhibited larger ΔT_{sol} in the infrared spectral region and a decreased T_{lum} in visible light. For VO_2 obtained with an annealing time of 60 min, T_{lum} and ΔT_{sol} are (56.45%, 14.95%), (46.45%, 17.15%) and (36.77%, 18.08%) for 1, 2 and 3 times of spin coating, respectively, exhibiting excellent optical properties. When the annealing time of VO_2 was extended to 150 min, the LSPR absorption edge (near 1200 nm) almost disappeared and the optical properties of the film dropped significantly, mainly due to the increase in VO_2 particle size. It is well-known that the M phase scatters light more strongly due to its larger refractive index, which can cause lower transmittance than the R phase. As result of this, there was a crosspoint in the transmittance curves found in Fig. S13d and e (ESI†) (circled by dashed line) which reduced ΔT_{sol}. Nevertheless, if the sizes of the VO_2(M) NPs were small enough, the difference in the light scattering between the M phase and R phase became negligible and the crosspoint disappeared (Fig. S13a–c, ESI†). Otherwise, the excitation of LSPR induced by sub-100 nm VO_2 NPs reduced the near-infrared region transmittance at high temperature, which was crucial to enhancing the optical performances of VO_2-based nanothermochromic films.[16,31,32]

The optical properties of VO_2@SiO_2 composite film

VO2 (M) is not thermodynamically stable in air and will be oxidized to V_2O_5 gradually over a long time. Coating a protective SiO_2 layer onto the surfaces of VO_2 particles is an effective way to solve the chemical and mechanical stability problem. This core–shell structure is optically transparent and can decrease the scattering caused by the refractive index mismatch between

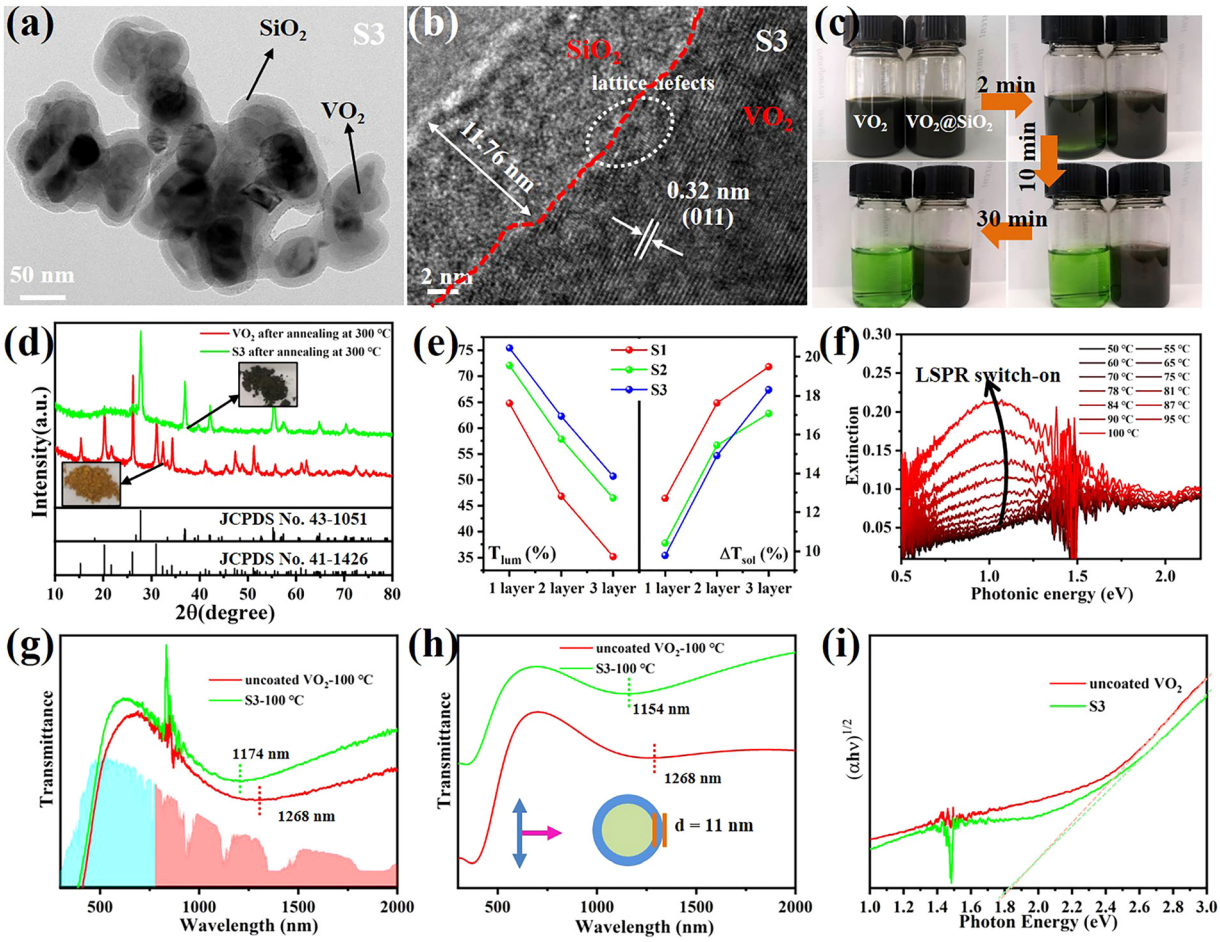

Fig. 4 (a) TEM image of S3. (b) HRTEM image of S3. Comparison of (c) acid corrosion and (d) oxidation resistance of VO_2 and VO_2@SiO_2 NPs. (e) Summarized optical performances of VO_2@SiO_2/PVP films with various spin coating times. (f) Temperature-dependent extinction spectra of VO_2@SiO_2/PVP film under increasing temperature. (g) Experimental and (h) simulated transmittance spectra of VO_2/PVP and VO_2@SiO_2/PVP films. (i) The relationship between $(\alpha h\nu)^{1/2}$ and $h\nu$ for the VO_2/PVP and VO_2@SiO_2/PVP films.

the nanoparticles and their polymer matrix.[33] Therefore, VO_2@SiO_2 core–shell NPs were prepared using the Stöber procedure, in which the shell thickness of the SiO_2 was controlled by the amount of TEOS used. The TEM images in Fig. 4a and Fig. S15 (ESI†) indicate that the thickness of the SiO_2 shell increased from 5.71 nm to 11.76 nm with the increased TEOS. From Fig. 4b, it can found that the SiO_2 shell is amorphous and the (011) crystal plane of VO_2(M) with an interplanar spacing of 0.32 nm was observed. Some lattice defects were observed which may be attributed to partial etching during the coating process. The enhancement of the acid corrosion resistance of the VO_2@SiO_2 NPs was confirmed using a comparison experiment. The uncoated VO_2 and S3 were added into a 1 M HCl solution at room temperature and Fig. 4c displays the color change of the suspension solution with time duration. The time-dependent transmittance at 550 nm of uncoated VO_2 and S3 suspension is shown in Fig. S16 (ESI†). The uncoated VO_2 was quickly etched and the suspension changed to green after 2 min and became completely transparent at about 10 min, indicating that the VO_2 NPs were dissolved in the acid solution. In contrast, S3 remained stable in acidic solutions from 0 min to 30 min and no visible color change was detected. The anti-oxidation of both samples was also investigated by annealing treatment in air. Fig. 4d shows the XRD patterns of uncoated VO_2 and S3 after annealing at 300 °C for 2 h in air. The uncoated VO_2 nanoparticle was almost totally oxidized to V_2O_5 and a yellow powder was obtained. For S3, there was no noticeable change in the XRD pattern and the color of the sample remained blue-black. Thus, coating an inert SiO_2 shell onto the surface of VO_2 dramatically improves the environmental durability and extends the lifetime of VO_2-based devices. Fig. S17a (ESI†) displays the DSC curves of VO_2@SiO_2 with various shell thicknesses. It was found that the T_c was reduced from 78.06 °C for uncoated VO_2 to 75.27, 72.47 and 72.11 °C for S1, S2 and S3, respectively. The incorporation of Si in the interface of VO_2 may increase the concentration of defects (see Fig. 4b), resulting in a decreased phase transition temperature. The SEM image of the surface morphology of S3/PVP film is presented in Fig. S17b (ESI†) and it was rougher than the surface of the VO_2/PVP film. The AFM image in the inset in Fig. S17b (ESI†) shows that the surface roughness was 47.309 nm and the cross-sectional image in Fig. S17c (ESI†) reveals that the thickness of the film was around 520 nm, while both values were larger than those of VO_2/PVP film.

The transmittance spectra of VO_2@SiO_2/PVP films at different temperatures are plotted in Fig. S18a–c (ESI†) and the calculated T_{lum} and ΔT_{sol} are summarized in Fig. 4e and Fig. S19 (ESI†). VO_2@SiO_2 with thinner shells exhibited higher ΔT_{sol} but lower T_{lum} when the same spin coating time was applied. For S3, the T_{lum} was 62.29% and the ΔT_{sol} was 14.91%, much higher than those of uncoated VO_2 NPs, demonstrating an enhancement of both T_{lum} and ΔT_{sol} and indicating a great potential for practical application in energy-efficient smart windows. Fig. 4f demonstrates the temperature-dependent LSPR on–off character and the enhanced LSPR intensity at higher temperatures due to the emergence of intermediate states during the metal–insulator transition. Furthermore, the existence of sub-50 nm VO_2 NPs was another key to the generation of LSPR. The LSPR peaks of S3 and uncoated VO_2 were at ~1174 and ~1268 nm, respectively (Fig. 4g). The blue-shift was mainly attributed to the SiO_2 shell and this was confirmed by the finite-difference time-domain (FDTD) simulations (Fig. 4h). According to the effective medium theory, the wavelength of the LSPR peak can be given by

$$\lambda_{SPR} = \lambda_{np}\sqrt{\frac{2+f}{1-f}\varepsilon_m + 1}$$

where $\lambda_{np} = 2\pi c/\omega_{np}$ for the VO_2(R) NPs, λ_{np} is the bulk plasma wavelength of VO_2(R), f is the filling factor, and ε_m is the dielectric constant of the surrounding medium of the VO_2(R) NPs. Apparently, λ_{SPR} was mainly determined by f and ε_m. As the temperature increased above T_c, the f of VO_2(R) gradually increased, resulting in the red-shift of λ_{SPR} during the heating process, which is in agreement with Fig. 4f. After coating with SiO_2, the f decreased compared to that of uncoated VO_2 and thus the λ_{SPR} exhibits a blue-shift in accordance with Fig. 4g.[34,35] The LSPR effect was totally quenched at room temperature, guaranteeing higher transmittance in the NIR range. With increasing temperature, the LSPR was enhanced gradually, resulting in increased absorption in the NIR region and finally ensuring the high optical modulation of the smart window. In addition, the blue-shifted LSPR peak of S3 makes its absorption peak match better with the peak of the solar irradiance spectrum, which will further enhance the thermochromic performance of VO_2 film.[36] It was reported that coating VO_2 with a metal oxide widens the optical band gap, but the optical band gap of S3 determined from the Tauc plot was similar to that of uncoated VO_2 (Fig. 4i).[37] Therefore, it could be concluded that the optimization of the LSPR peak position through the SiO_2 shell was the most dominant factor in improving the thermochromic performance of VO_2@SiO_2 film.

To evaluate the energy-saving effect of VO_2@SiO_2 thermochromic film under outdoor conditions, we built a simple house model using polystyrene foam and pasted thermochromic film in its roof, as depicted in Fig. 5a. The temperature inside the house was monitored by a thermocouple and another reference model was mounted with a bare glass window. The temperature change curve of the test environment is displayed in Fig. S20a (ESI†). Fig. 5b shows that the in-house temperatures of both model houses increased and reached the maximum temperature at noon with continuous exposure to solar irradiation. Notably, the in-house temperature of the model with the thermochromic film increased more slowly and a maximum 15.1 °C temperature difference was seen between these two models, indicating the effective solar energy regulation of VO_2@SiO_2 film. The model house experiment was also conducted in winter and the results are displayed in Fig. S20b and c (ESI†). Taking into account both annual heating and annual cooling energy, this film may do well in reducing energy consumption all year round. Fig. 5c displays recent reports on the ΔT_{sol} and T_{lum} of VO_2 obtained under different

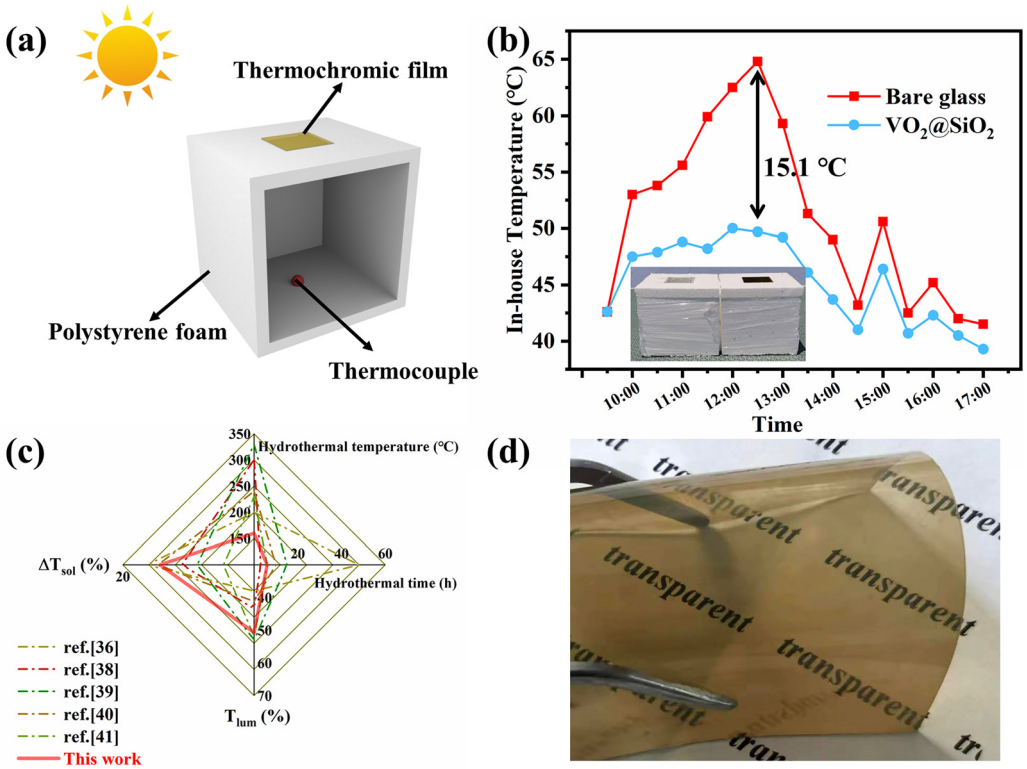

Fig. 5 (a) Schematic of the model house. (b) In-house temperature profiles of model houses (the inset shows the digital image of model houses used for the experiments). (c) Reported ΔT_{sol} and T_{lum} of VO_2 obtained under different hydrothermal times and temperatures. (d) A digital image of the flexible VO_2 film.

hydrothermal times and temperatures. For the one-step hydrothermal method, a critical hydrothermal temperature above 240 °C or even 300 °C is essential.[38,39] For the two-step hydrothermal method, the hydrothermal temperature could be lower than 240 °C but needs to be at least 200 °C.[36,40,41] It is obvious the hydrothermal conditions of our work were mild and effective. Moreover, as for the thermochromic performance, the prepared VO_2@SiO_2/PVP film achieved a good balance between ΔT_{sol} (18.30%) and T_{lum} (50.69%), which is desirable for the application of VO_2-based films as smart windows. Fig. 5d shows the VO_2@SiO_2/PVP film cast onto a PET substrate, indicating the potential application of VO_2 in some promising flexible devices.

4. Conclusion

In summary, we reported an efficient and mild hydrothermal method for the preparation of lepidocrocite VOOH ultrafine NPs. The influence of hydrothermal conditions on the hydrothermal products was studied and the characterizations confirmed that the formation of VOOH NPs was induced by a Kirkendall diffusion process. The obtained VOOH could be further transformed into VO_2(M) after annealing treatment, leading to well crystalline VO_2 NPs with optimum thermochromic and plasmonic properties. Coating VO_2 NPs with an inert SiO_2 shell not only improved the environmental tolerance of VO_2, but also enhanced the optical modulation of the VO_2 film, which was attributed to the blue-shift of the LSPR peak. The optimal ΔT_{sol} and T_{lum} were 14.91% (~15%) and 62.29% (> 60%), offering new opportunities for VO_2-based energy-efficient smart windows.

Author contributions

L. W. and A. T. fabricated the samples, finished the data measurement and prepared the manuscript. M. L., X. H. and G. L. conceived the idea and revised the paper. L. L., Z. H., X. L., J. Y, S. X. and F. Z. coordinated this study and checked the literature. A. Z., J. Z., T. J. and Y. X. discussed the results and commented on the manuscript.

Conflicts of interest

There are no conflicts to declare.

Acknowledgements

This work was supported by the HFIPS Director's Fund (Grant No. YZJJ202202-CX, YZJJ2022QN28, YZJJ202308-TS, YZJJ202312-TS, YZJJ-GGZX-2022-01); Zhulin Huang would like to thank the Natural Science Foundation of China (Grant No. 52222208, 52072373).

References

1 S. Wang, T. Jiang, Y. Meng, R. Yang, G. Tan and Y. Long, *Science*, 2021, **374**, 1501–1504.
2 Q. Lei, W. Yu, G. Xie, Y. Li, C. Wu, G. Jiang, Y. Zhou and H. Xie, *Sol. RRL*, 2023, **7**, 2200990.
3 G. Chen, K. Wang, J. Yang, J. Huang, Z. Chen, J. Zheng, J. Wang, H. Yang, S. Li, Y. Miao, W. Wang, N. Zhu, X. Jiang, Y. Chen and J. Fu, *Adv. Mater.*, 2023, **35**, 2211716.
4 H. Zhang, J. Feng, F. Sun, D. Zhou, G. Cao, S. Wang, X. Hu, J. Ma, F. Su, Y. Tian and Y. Tian, *Adv. Mater. Technol.*, 2023, **8**, 2201688.
5 J. Liu, R. Yang, J. Zhang, Q. Tao, A. Li, Z. Liu, Y. Su and Y. Liu, *Sol. Energy Mater. Sol. Cells*, 2023, **249**, 112048.
6 E. Poloni, A. Rafsanjani, V. Place, D. Ferretti and A. R. Studart, *Adv. Mater.*, 2022, **34**, 2104874.
7 M. Liu, X. Li, L. Li, L. Li, S. Zhao, K. Lu, K. Chen, J. Zhu, T. Zhou, C. Hu, Z. Lin, C. Xu, B. Zhao, G. Zhang, G. Pei and C. Zou, *ACS Nano*, 2023, **17**, 9501–9509.
8 T. Zhang and Q. Li, *J. Solid State Chem.*, 2022, **311**, 123117.
9 J. Zhang, X. Sun, T. Wang, W. Xu, G. Luo, Y. Wang and C. Zhou, *Opt. Mater.*, 2023, **136**, 113498.
10 Y. Ke, Y. Tan, C. Feng, C. Chen, Q. Lu, Q. Xu, T. Wang, H. Liu, X. Liu, J. Peng and Y. Long, *Appl. Energy*, 2022, **315**, 119053.
11 Z. Li, C. Cao, M. Li, L. Wang, D. Zhu, F. Xu, A. Huang, P. Jin, L. Yu and X. Cao, *ACS Appl. Mater. Interfaces*, 2023, **15**, 9401–9411.
12 L. Zhang, J. Yao, Y. Guo, F. Xia, Y. Cui, B. Liu and Y. Gao, *Ceram. Int.*, 2018, **44**, 19301–19306.
13 C. Wang, H. Xu, C. Wang, T. Liu, S. Yang, Y. Nie, X. Guo, X. Ma and X. Jiang, *J. Alloys Compd.*, 2021, **877**, 159888.
14 L. Liu, F. Cao, T. Yao, Y. Xu, M. Zhou, B. Qu, B. Pan, C. Wu, S. Wei and Y. Xie, *New J. Chem.*, 2012, **36**, 619–625.
15 S. Guan, A. Rougier, O. Viraphong, D. Denux, N. Penin and M. Gaudon, *Inorg. Chem.*, 2018, **57**, 8857–8865.
16 K. Li, M. Li, C. Xu, Y. Luo and G. Li, *J. Alloys Compd.*, 2020, **816**, 152655.
17 C. Z. Wu, Y. Xie, L. Y. Lei, S. Q. Hu and C. Z. OuYang, *Adv. Mater.*, 2006, **18**, 1727–1732.
18 J. Zhang, R. Cui, C. Gao, L. Bian, Y. Pu, X. Zhu, X. A. Li and W. Huang, *Small*, 2019, **15**, 1904688.
19 H. Shi, H. Liang, F. Ming and Z. Wang, *Angew. Chem., Int. Ed.*, 2017, **56**, 573–577.
20 J. Yao, H. Zhang, Z. Zhao, Z. Zhu, J. Yao, X. Zheng and Y. Yang, *Dalton Trans.*, 2021, **50**, 3867–3873.
21 W. Xiao, S. Oh, T. V. M. Sreekanth, J. Kim and K. S. Yoo, *ACS Appl. Mater. Interfaces*, 2022, **14**, 34802–34813.
22 X. Cao, N. Wang, J. Y. Law, S. C. J. Loo, S. Magdassi and Y. Long, *Langmuir*, 2014, **30**, 1710–1715.
23 C. Wu, X. Zhang, B. Ning, J. Yang and Y. Xie, *Inorg. Chem.*, 2009, **48**, 6044–6054.
24 Y. Xu, L. Zheng and Y. Xie, *Dalton Trans.*, 2010, **39**, 10729–10738.
25 M. Fan, D. Liao, M. F. A. Aboud, I. Shakir and Y. Xu, *Angew. Chem., Int. Ed.*, 2020, **59**, 8247–8254.
26 B. Shen, L. Huang, J. Shen, X. Hu, P. Zhong, C. Y. Zheng, C. Wolverton and C. A. Mirkin, *ACS Nano*, 2023, **17**, 4642–4649.
27 J. Pi, C.-B. Li, R.-Y. Sun, L.-Y. Li, F. Wang, F. Song, J.-M. Wu, X.-L. Wang and Y.-Z. Wang, *Compos. Commun.*, 2022, **32**, 101167.
28 Z. Li, S. Zhao, Z. Shao, H. Jia, A. Huang, P. Jin and X. Cao, *Chem. Eng. J.*, 2022, **447**, 137556.
29 X. Li, C. Cao, C. Liu, W. He, K. Wu, Y. Wang, B. Xu, Z. Tian, E. Song, J. Cui, G. Huang, C. Zheng, Z. Di, X. Cao and Y. Mei, *Nat. Commun.*, 2022, **13**, 7819.
30 L. H. Molloro, S. Tain, N. Belachew, K. A. Owusu and X. Zhao, *RSC Adv.*, 2021, **11**, 13556–13563.
31 W. Li, S. Ji, K. Qian and P. Jin, *J. Colloid Interface Sci.*, 2015, **456**, 166–173.
32 X. Wang, M. Li, Q. Wang, J. Zhang, J. Shi, Y. Lu and G. Li, *Eur. J. Inorg. Chem.*, 2020, 1783–1789.
33 Y.-Q. Li, S.-Y. Fu, Y. Yang and Y.-W. Mai, *Chem. Mater.*, 2008, **20**, 2637–2643.
34 J. Song, Y. Zhao, L. Sun, Q. Luo, H. Xu, C. Wang, H. Xin, W. Wu and F. Ma, *Ceram. Int.*, 2022, **48**, 15868–15876.
35 S. Long, X. Cao, R. Huang, F. Xu, N. Li, A. Huang, G. Sun, S. Bao, H. Luo and P. Jin, *ACS Appl. Mater. Interfaces*, 2019, **11**, 22692–22702.
36 Z. Du, M. Li, F. Zou, Y. Song, S. Xu, L. Wu, L. Li and G. Li, *ACS Appl. Nano Mater.*, 2022, **5**, 12972–12979.
37 Y. Chen, X. Zeng, J. Zhu, R. Li, H. Yao, X. Cao, S. Ji and P. Jin, *ACS Appl. Mater. Interfaces*, 2017, **9**, 27784–27791.
38 X. Zhao, J. Sun, Z. Guo, J. Su, T. Liu, R. Hu, W. Yao and X. Jiang, *Chem. Eng. J.*, 2022, **446**, 137308.
39 Z. Chen, Y. Tang, A. Ji, L. Zhang and Y. Gao, *ACS Appl. Nano Mater.*, 2021, **4**, 4048–4054.
40 J. Kang, J. Liu, F. Shi, Y. Dong, X. Song, Z. Wang, Z. Tian, J. Xu, J. Ma and X. Zhao, *Appl. Surf. Sci.*, 2022, **573**, 151507.
41 Z. Zhao, Y. Liu, D. Wang, C. Ling, Q. Chang, J. Li, Y. Zhao and H. Jin, *Sol. Energy Mater. Sol. Cells*, 2020, **209**, 110443.